Supporting Information for

Aqueous-phase photochemical oxidation and direct photolysis of vanillin—a model compound of methoxy-phenols from biomass burning

Y.J. Li[1], D.D. Huang[2], H.Y. Cheung[1], A.K.Y. Lee[3] and C.K. Chan[1,2]

[1]Division of Environment, Hong Kong University of Science and Technology, Hong Kong, China
[2] Department of Chemical and Biomolecular Engineering, Hong Kong University of Science and Technology, Hong Kong, China
[3]Department of Chemistry, University of Toronto, Toronto, Canada

Manuscript submitted to *Atmospheric Chemistry and Physics*, 14th, Feb., 2014.

Correspondence to: C.K. Chan (keckchan@ust.hk)

1. Experimental setup

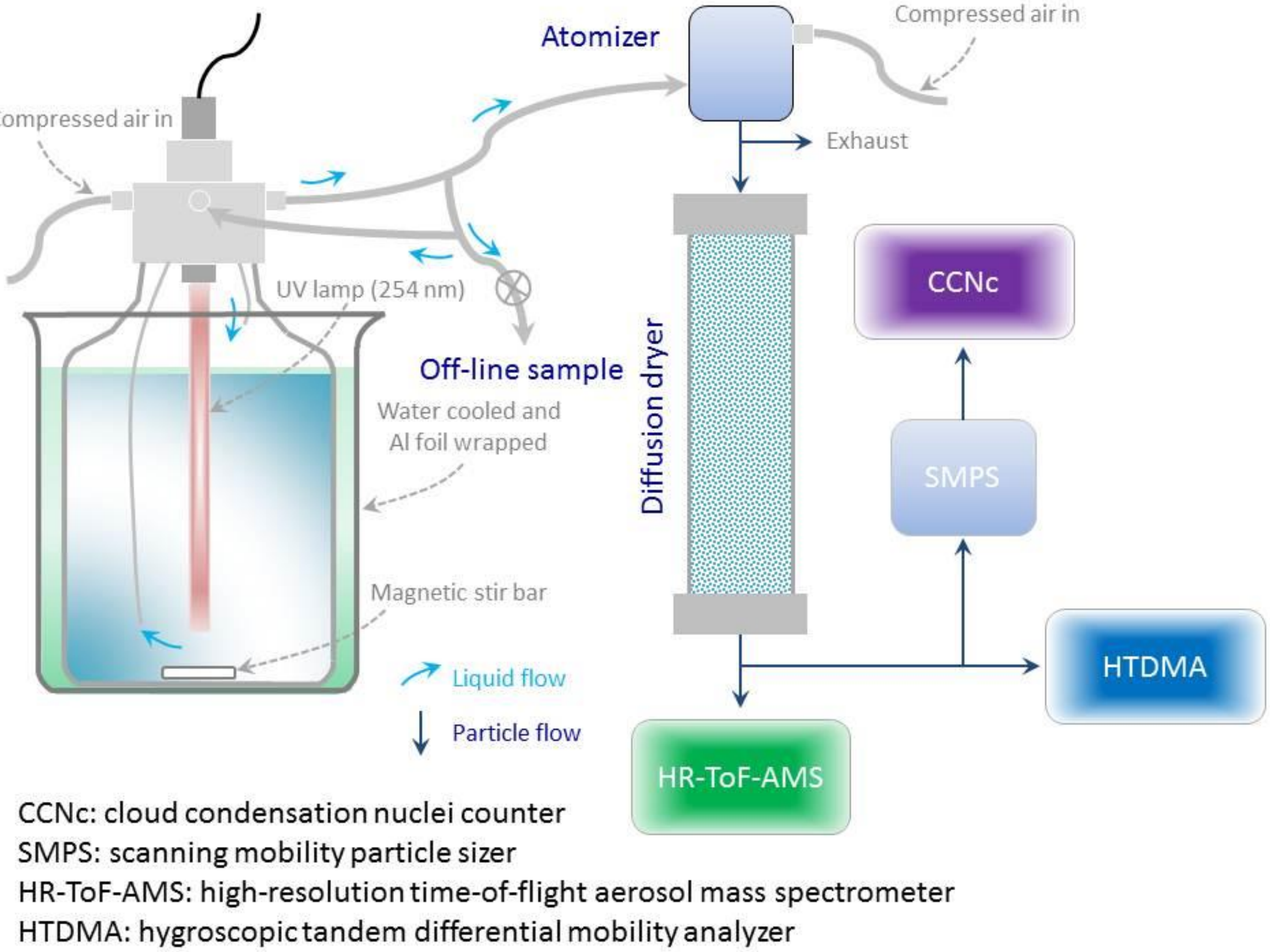

Figure S1. Experimental setup for the aqueous-phase reactions.

2. Examples of control experiments (C_1 to C_4)

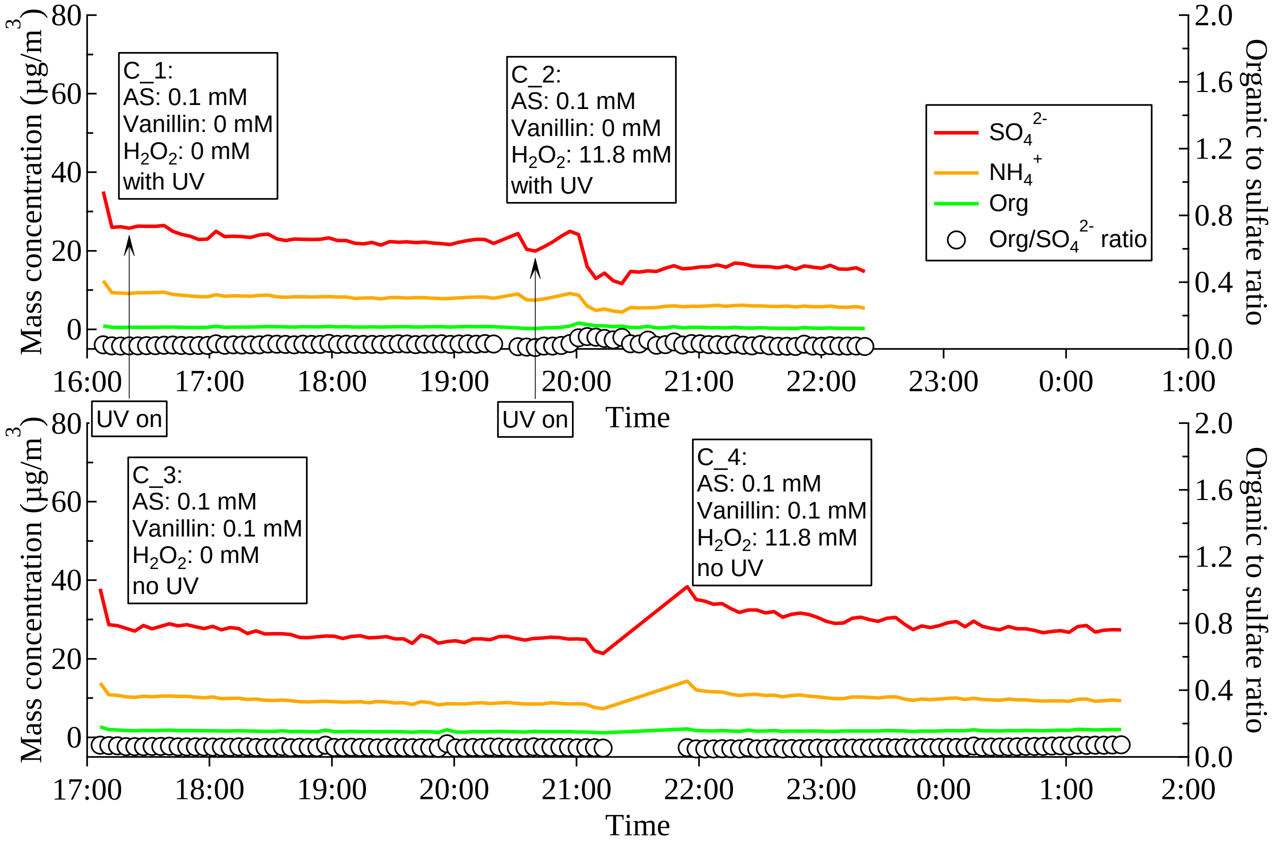

Figure S2. Concentrations of species and ratios of organics to sulfate during control experiments C_1 to C_4 (Table 1).

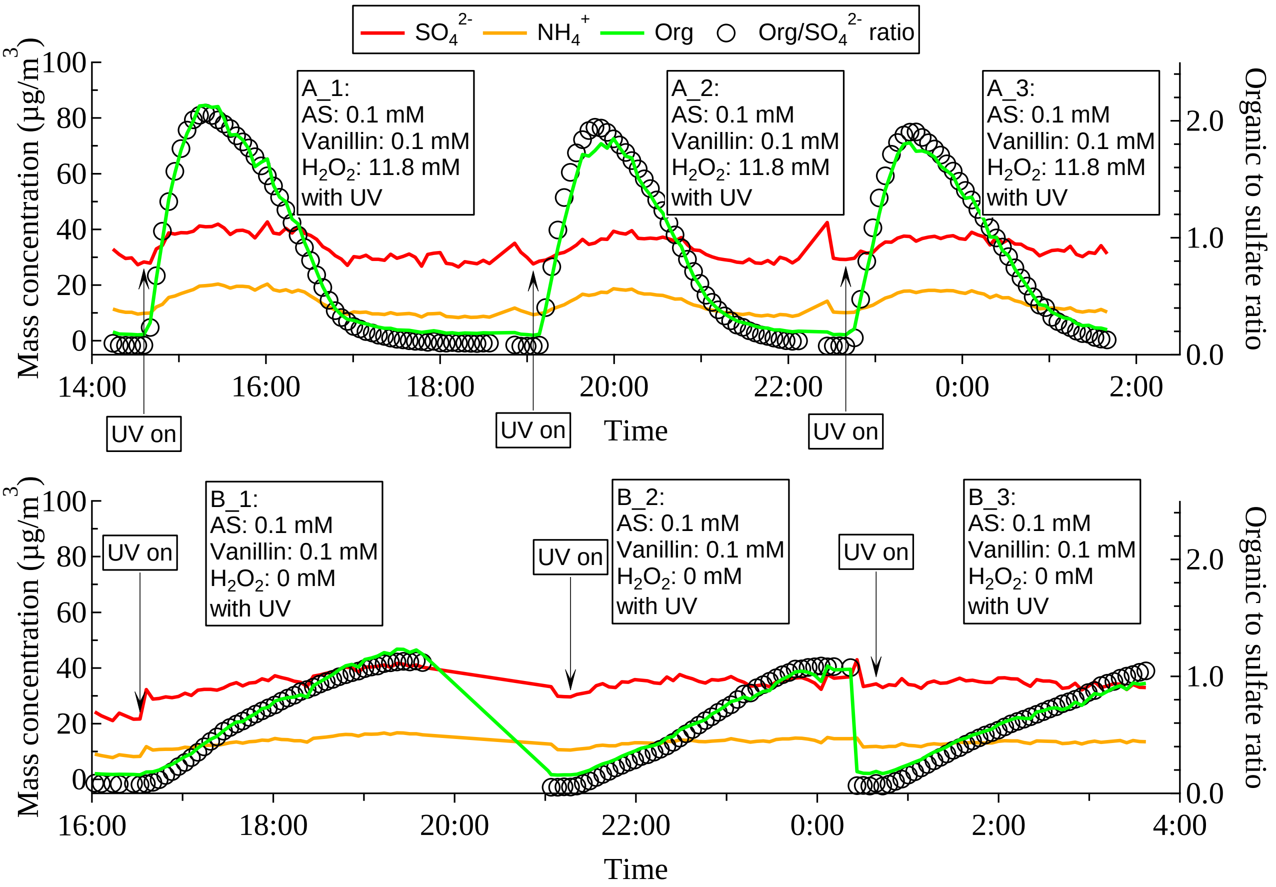

Figure S3. Species concentrations and organics to sulfate ratios in experiments A_1 to A_3, and B_1 to B_3. The experimental conditions are specified in each box indicating the experiment number.

3. AMS analysis

3.1 Modification of the fragmentation table

In the default fragmentation table (Aiken et al., 2007;Allan et al., 2004), the signals of ions H_2O^+ and CO^+ are related to that of CO_2^+ with coefficients of 0.225 and 1.0, respectively. These coefficients work well for ambient data, but were found to be somewhat different in laboratory studies (Chen et al., 2011;Li et al., 2011b;Sun et al., 2010). Several approaches can be used to obtain more representative coefficients for these ions (Li et al., 2011b). Briefly, one can use the particle time-of-flight (pToF) data to exclude signal contribution from gaseous H_2O and CO (Zhang et al., 2005), and use high-resolution data from W mode to exclude interfering ions such as those from NH_4^+ (Li et al., 2011b). For our experiments in which a dryer was used (little contribution from gaseous water) and no excess CO would be generated (as in burning experiments), the pToF correction was not necessary. But the correlations of high-resolution data would be helpful in determining the coefficients. Shown below in Figure S4 are those correlations in different runs of experiments. For H_2O^+ vs. CO_2^+, slopes close to unity were determined. But it is believed that approximately half of these H_2O^+ signals come from strongly bound particulate water, leaving the other half from organics (Chen et al., 2011). Therefore, a factor of 0.5 was applied to these slopes to obtain final coefficients between H_2O^+ and CO_2^+. For CO^+ vs. CO_2^+, the slopes were directly used as the coefficients. Table S1 summarizes those coefficients for different runs, with the default values also given for reference.

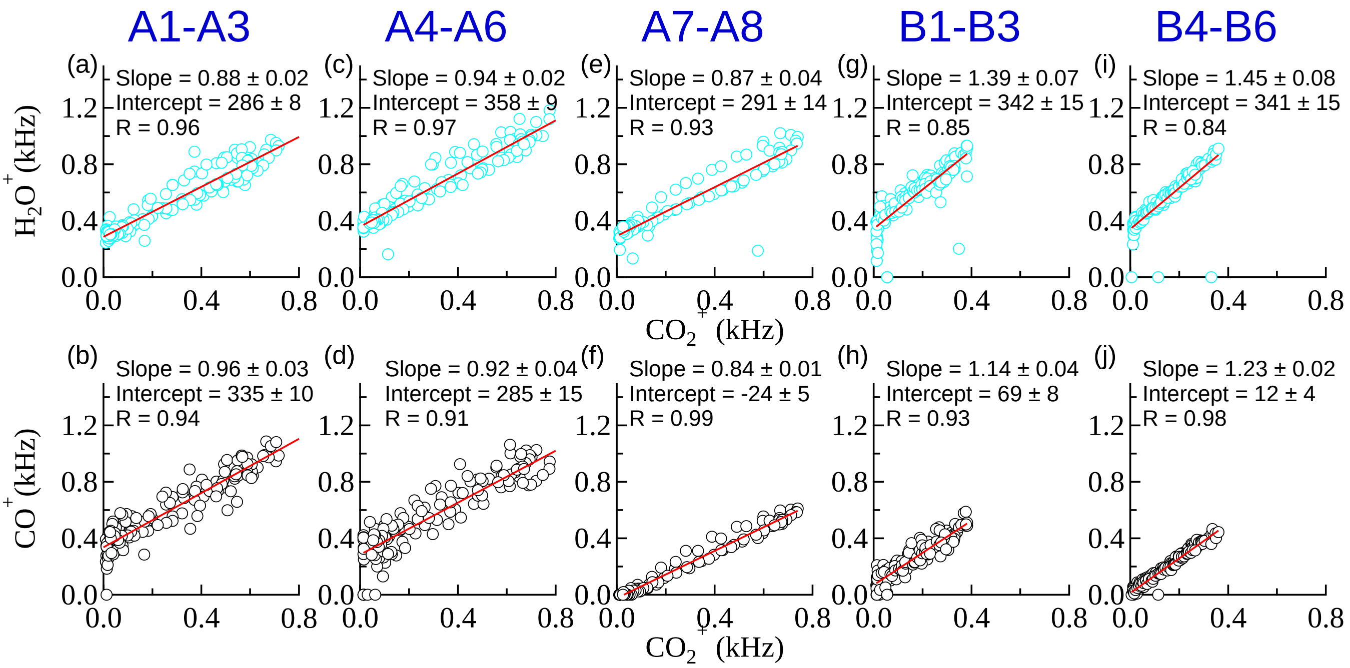

Figure S4. Relationships of ion signal intensities (kHz) of H_2O^+ vs. CO_2^+ and CO^+ vs. CO_2^+ from high-resolution mass spectra obtained in W mode.

Table S1. Coefficients of H_2O^+ and CO^+ signals as related to the CO_2^+ signal used in the fragmentation table. The default values are also shown for reference. Experimental runs indicated by experiment numbers (e.g., A_1-A_3) are listed in Table 1.

Experiment	**Default**	**A_1-A_3**	**A_4-A_6**	**A_7-A_8**	**B_1-B_3**	**B_4-B_6**
Org18/Org44 or HROrgH_2O^+/HROrgCO_2^+	0.225	0.44	0.57	0.44	0.69	0.72
Org28/Org44 or HROrgCO^+/HROrgCO_2^+	1.00	0.96	0.92	0.82	1.14	1.23

3.2 Background subtraction

Trace amounts of impurities in water can contribute to organic mass spectra. Although their mass is generally less than 5%, their contribution to specific organic ions in the mass spectra could interfere with real signals from reaction products. For example, the peak at 137 as a tracer of the ring-retaining structure in Figure 2 needs to be scrutinized to make sure it is not from the background. Thus, for mass spectra obtained and shown in Figure 2, background subtraction was performed. Assuming the impurities also evolved during the photochemical oxidation and direct photolysis as did the target reactant, time-specific background subtraction was performed. For example, the mass spectrum obtained at 40 minutes in condition (A) was obtained by subtracting the mass spectrum in experiment A_2 at 40 minutes from a mass spectrum in condition (A) and that in experiment C_1 at 40 minutes from a mass spectrum in condition (A), and so on.

4. Estimation of the OH radical concentration

During the photochemical oxidation experiments, OH radical was generated by photolysis of H_2O_2. To determine the H_2O_2 decay rate during photolysis, the H_2O_2 concentration was measured by a colorimetric method (Allen et al., 1952). A calibration curve is shown in Figure S5.

The H_2O_2 decay rate was determined in “neutral” (ammonium sulfate, 0.1 mM) or acidic (ammonium bisulfate, 0.1 mM) conditions. The decay rate was relatively independent of pH, as suggested by Tan et al. (Tan et al., 2009). From these decay experiments, a decay rate (k_{obs}) of 1.9×10^{-4} s^{-1} was determined (Figure S6, green dotted curve), which is comparable to that in a previous study (see Table S2) that used the same brand and model of UV lamp (An et al., 2001). However, if this decay rate is taken as the photolysis rate constant (k_1, Table S2), the modeled H_2O_2 decay (see below) after taking into account reactions with other reactive oxygen species (such as OH, HO_2 radicals etc., reactions 2-7 in Table S2) would not match the experimental decay of H_2O_2 (see Figure S6, red curve). After a few iterations, it was determined that a photolysis rate constant (k_1) of 1.0×10^{-4} s^{-1} should be used instead (Figure S6, blue curve).

Rate constants (k_2 to k_6) for reactions of other reactive oxygen species are adopted from the literature as shown in Table S2. The rate constant (k_7) of the oxidation reaction of organics (Org) by OH radicals is assumed to be 1×10^8 $M^{-1}s^{-1}$ (Lee et al., 2012). Reaction rate expressions were thus set up for these reactions. The concentrations of the species H_2O_2, HO_2, OH, and Org were then solved with the help of the POLYMATH (Willimantic, CT) ordinary differential equation (ODE) solver via two approaches: (1) assuming a pseudo-steady-state for OH radicals, and (2) solving stiff ODEs without a constraint on OH radicals.

For approach (1), the expression for OH concentration is shown in Eq. S1 and set to 0.

$$\frac{\mathrm{d[OH]}}{\mathrm{dt}} = 2 \times k1[H_2O_2] - k2[OH][H_2O_2] + k3[HO_2][H_2O_2] - k5[OH][HO_2] - 2 \times k6[OH][OH] - k7[Org][OH] = 0 \qquad \text{Eq. S1}$$

Thus

$$2 \times k6[OH]^2 + (k2[H_2O_2] + k5[HO_2] + k7[Org]) \times [OH] - (2 \times k1[H_2O_2] + k3[HO_2][H_2O_2]) = 0 \qquad \text{Eq. S2}$$

Solving this quadratic equation:

$$[\mathrm{OH}] = \frac{-(k2[H_2O_2]+k5[HO_2]+k7[Org]) \pm \sqrt{(k2[H_2O_2]+k5[HO_2]+k7[Org])^2+4\times2\times k6\times(2\times k1[H_2O_2]+k3[HO_2][H_2O_2])}}{2\times2\times k6} \qquad \text{Eq. S3}$$

The expressions of other species (H_2O_2, HO_2, and Org) are shown as below.

$$\frac{\mathrm{d}[H_2O_2]}{\mathrm{dt}} = -k1[H_2O_2] - k2[OH][H_2O_2] - k3[HO_2][H_2O_2] + k4[HO_2][HO_2] + k6[OH][OH] \qquad \text{Eq. S4}$$

$$\frac{\mathrm{d}[HO_2]}{\mathrm{dt}} = k2[OH][H_2O_2] - k3[HO_2][H_2O_2] - 2 \times k4[HO_2][HO_2] - k5[OH][HO_2] \qquad \text{Eq. S5}$$

$$\frac{\mathrm{d}[Org]}{\mathrm{dt}} = -k7[Org][OH] \qquad \text{Eq. S6}$$

Replacing all the [OH] in Eq. S4 – Eq. S6 with the positive solution of the quadratic equation for the pseudo-steady-state assumption for OH radicals (Eq. S3), the concentrations of H_2O_2, HO_2, and Org as a function of time were obtained by solving the ODEs (Eq. S4 – Eq. S6). The OH concentration was then back-calculated from Eq. S3. Initial concentrations of 10^{-3} to 10^{-6} M were tested for Org, and the OH concentration ranged from 6.5 – 7.8 × 10^{-12} M. An OH radical concentration of 7.2 × 10^{-12} M was then chosen, with the Org concentration of 10^{-4} M (as the initial concentration of VL added).

For approach (2), Eq. S1 and Eq. S4 – Eq. S6 were included in the calculation without any constraint on OH radicals. The set of ODEs was stiff and thus an option of stiff ODE calculation was used in POLYMATH was used to solve the species concentrations of H_2O_2, HO_2, Org, as well as OH, as a function of time. OH concentration was estimated to be 7.0 × 10^{-12} M, showing little difference from that obtained by approach (1).

Figure S7 shows the OH concentrations estimated by approach (1) with a pseudo-steady-state assumption for OH radicals and approach (2) without any constraint on OH radicals. Two k_1 values were used for approach (1): the one determined from the H_2O_2 decay experiment ($k_1 = k_{obs}$ = 1.9 × 10^{-4} s^{-1}, red curve in Figure S7), and (b) the one determined from the model (k_1 = 1.0 × 10^{-4} s^{-1}, blue curve in Figure S7) by taking into account other reactions (reactions 2-6 in Table S2). A k_1 value of 1.0 × 10^{-4} s^{-1} was used for approach (2) (green curve in Figure S7). With a k_1 value of 1.0 × 10^{-4} s^{-1}, the two approaches resulted in very similar and quite steady OH concentrations, while using the H_2O_2 decay constant as the photolysis constant leads to a factor of two overestimation of the OH radical concentration. An OH concentration of 7.0 × 10^{-12} M, which is one order of magnitude higher than that in cloud water, but close to that in wet aerosol particles (Ervens et al., 2013), was thus used.

By using the OH concentration of 7.0 × 10^{-12} M, the bimolecular reaction rate constant between VL and OH was determined to be 3.9 × 10^8 $M^{-1}s^{-1}$ by simply dividing the decay rate of VL in condition (A) (2.7 × 10^{-3} s^{-1}, see Figure 4) by the steady-state OH concentration (7.0 × 10^{-12} M). Alternatively, the same model with all the reactions in Table S2 was also run by varying k_7 (as the k_{OH} of organics, VL in this case), as in Figure S8. Regardless of which approach was used (OH concentration constrained or not), the modeled VL decay matched the measured one when k_7 was set to 4 × 10^8 $M^{-1}s^{-1}$. Therefore, the bimolecular reaction rate constant of VL and OH reaction (k_{OH}) was determined to be ~4 × 10^8 $M^{-1}s^{-1}$.

Table S2. Reactions and rate constants for aqueous-phase reactions involving reactive oxygen species (H_2O_2, HO_2, OH, etc.) as well as organics.

	Reaction	Rate constant	References
1	$H_2O_2 + h\nu \rightarrow 2OH$	$k_1 = 1.1 \times 10^{-4}\ s^{-1}$	Tan et al. 2009 (Heraeus Noblelight Hg lamp, 254 nm)
		$k_1 = 1.6 \times 10^{-4}\ s^{-1}$	Perri et al. 2009 (Strahler Hg lamp, 254 nm)
		$k_{obs} = 1.9 \times 10^{-4}\ s^{-1}$ **$k_1 = 1.0 \times 10^{-4}\ s^{-1}$**	**This study (UVP Pen-Ray lamp, 254 nm)**
		$k_{obs} = 2.0 \times 10^{-4}\ s^{-1}$	An et al. 2001 (UVP Pen-Ray lamp, 254 nm)
2	$OH + H_2O_2 \rightarrow HO_2 + H_2O$	**$k_2 = 2.7 \times 10^7\ M^{-1}s^{-1}$**	**Sander and Crutzen, 1996; Warneck, 1999; Perri et al. 2009**
3	$HO_2+H_2O_2 \rightarrow OH + H_2O + O_2$	**$k_3 = 3.7\ M^{-1}s^{-1}$**	**Tan et al. 2009; Lee et al. 2012**
4	$HO_2 + HO_2 \rightarrow H_2O_2 + O_2$	**$k_4 = 9.7 \times 10^5\ M^{-1}s^{-1}$**	**Sander and Crutzen, 1996; Warneck, 1999; Perri et al. 2009**
5	$OH + HO_2 \rightarrow H_2O + O_2$	**$k_5 = 7.1 \times 10^9\ M^{-1}s^{-1}$**	**Sander and Crutzen, 1996; Warneck, 1999; Perri et al. 2009**
6	$OH + OH \rightarrow H_2O_2$	**$k_6 = 5.5 \times 10^9\ M^{-1}s^{-1}$**	**Sander and Crutzen, 1996; Warneck, 1999; Perri et al. 2009**
7	Org + OH → oxyOrg	**$k_7 = 1 \times 10^8\ M^{-1}s^{-1}$**	**Lee et al. 2012**

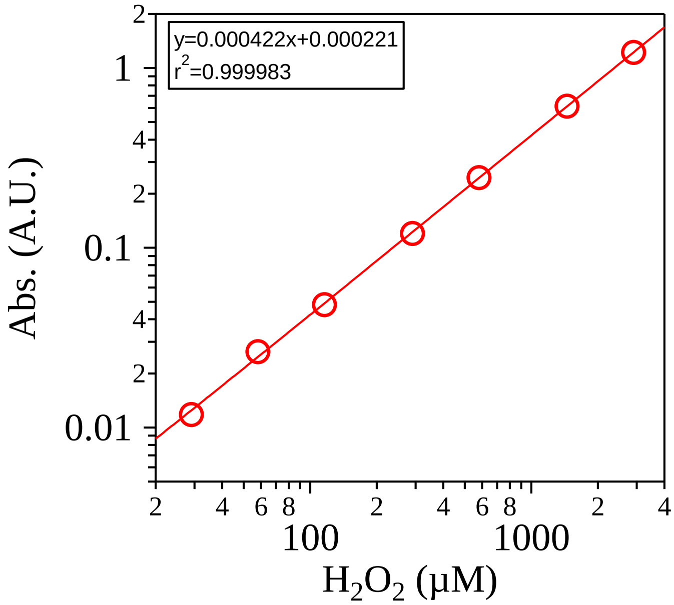

Figure S5. A typical calibration curve for H_2O_2.

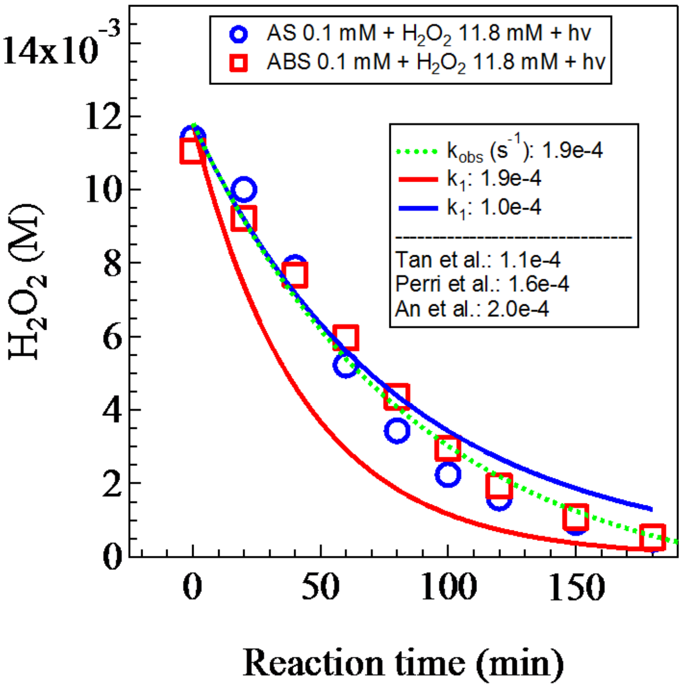

Figure S6. H_2O_2 decay experiments under “neutral” (blue circles) and acidic (red squares) conditions. The green dotted curve is the fitted (exponential decay) curve for data points under both “neutral” and acidic conditions, resulting in a decay rate of $k_{obs} = 1.9 \times 10^{-4}$ s^{-1}. The red solid curve is the calculated H_2O_2 decay from reactions 1-6 with $k_1 = k_{obs}$. The blue solid curve is the calculated H_2O_2 decay from reactions 1-6 with $k_1 = 1.0 \times 10^{-4}$ s^{-1}.

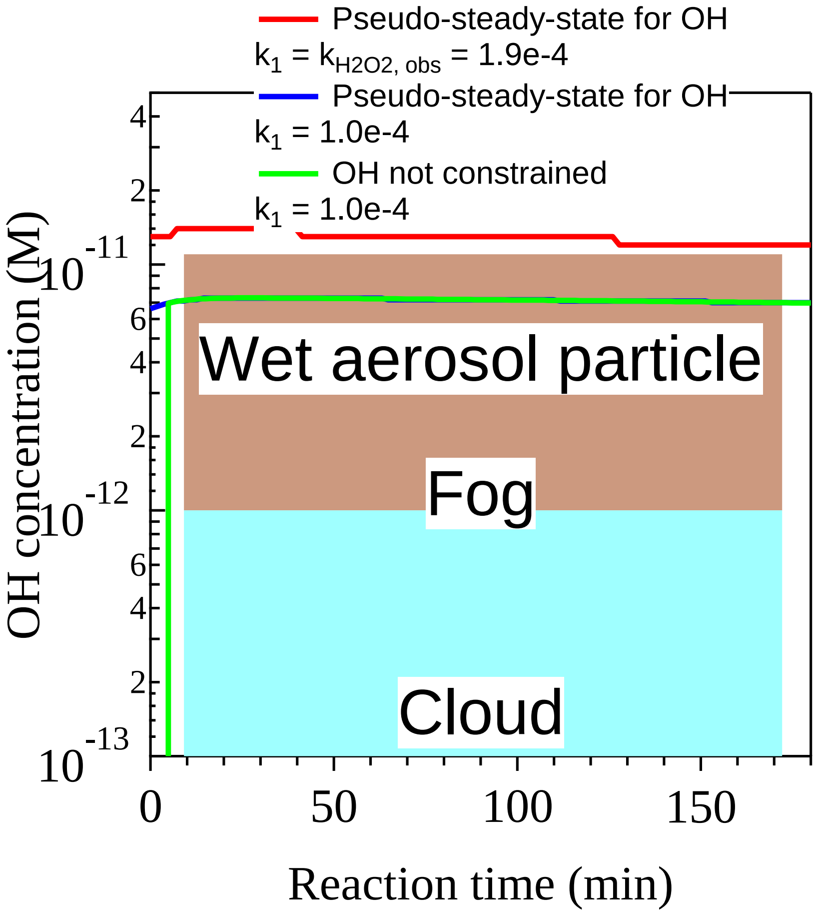

Figure S7. OH concentrations estimated from two approaches and with k_1 set to different values. Also shown are typical ranges of OH concentration under ambient conditions (Ervens et al., 2011;Ervens et al., 2013;Warneck, 2003).

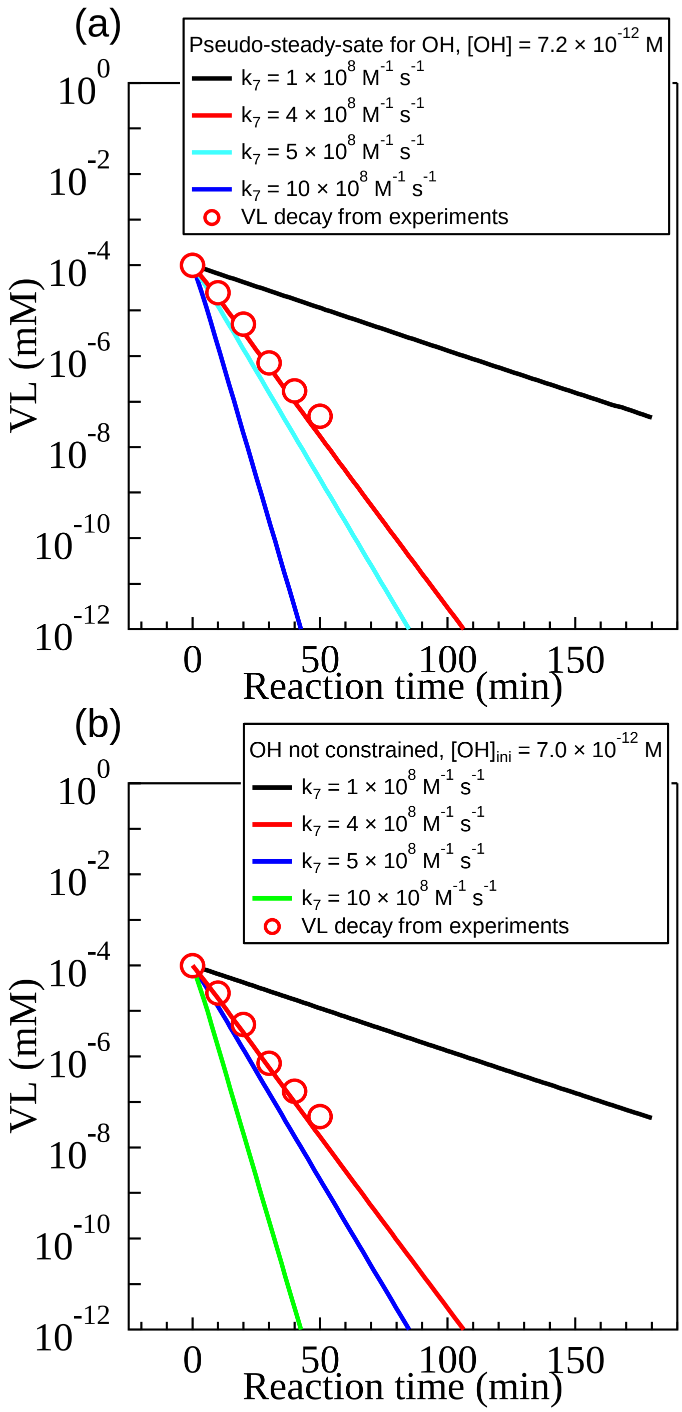

Figure S8. VL decay modeled from two approaches: pseudo-steady-state for OH radicals (a), and no constraint on OH radicals (b). Different values of k_7 in Table S2 were tested in both approaches to see which one would give the experimentally observed VL decay (red circles).

5. Off-line analyses

5.1 Ultra-performance liquid chromatography with diode array detector (UPLC-DAD)

Aqueous samples at different time intervals from experiments A_1 to A_3, and those from B_1 to B_3 (see Table 1), as well as VL and vanillic acid (VA) aqueous solutions with known concentrations were analyzed by UPLC-DAD (Waters, Milford, MA). A Waters ACQUITY UPLC HSS C18 column (1.8 µg, 2.1 mm × 100 mm) was used. A solvent gradient with solvent A as 0.02 vol% trifluoroacetic acid (TFA) in water and solvent B as 0.02 vol% TFA in acetonitrile was used for the separation. The gradient was 35% B in the first 0.2 minutes, increased to 90% B in the next 2.8 minutes, stayed at 90% B for 1 minute, and then decreased to 35% B in the next 0.2 minutes. The flow rate was 0.45 mL/min. Two channels with UV absorption of 254 nm and 300 nm were used for the detection. VL was quantified with the 300 nm channel while VA was quantified with the 254 nm channel. Typical chromatograms (UV absorption at 300 nm) and calibration curves are shown in Figure S9 and Figure S10, respectively.

VA had a retention time of ~1.2 minutes, while VL had a retention time of ~1.4 minutes (Figure S9-a). Sample from condition (A) showed a strong VL peak at 10 minutes (Figure S9-b), but the peak became very small at later time intervals (Figures S9-c, and –d). There was a very small amount of VA at 10 minutes, and its peak at later time intervals became undetectable in 300-nm chromatograms and very small in 254-nm chromatograms (the wavelength for its quantification, not shown). There were a number of peaks with retention times shorter than 1.2 minutes, probably due to the formation of other products (e.g., small carboxylic acids). Since most of them were not well separated, they were not quantified. Samples from condition (B) showed a strong VL peak at 1.4 minutes throughout the course of the 3-hour experiments, in accordance with the slow reactions of VL under condition (B). Some small peaks at 1.2 minutes (VA) and at even shorter retention times were observed. They might also be those small carboxylic acids formed at later time intervals, although their amounts would be much smaller than in condition (A). This also supports the analysis of the O:C ratio (see main text Section 3.2), which concludes that the identified high-molecular-weight products (see discussion later on UPLC-ToF-MS) cannot explain the relatively high O:C ratio (~1.0 at the end of the experiments, see Figure 3-B) and certain amounts of small and highly oxygenated products were also formed later in the experiments under condition (B).

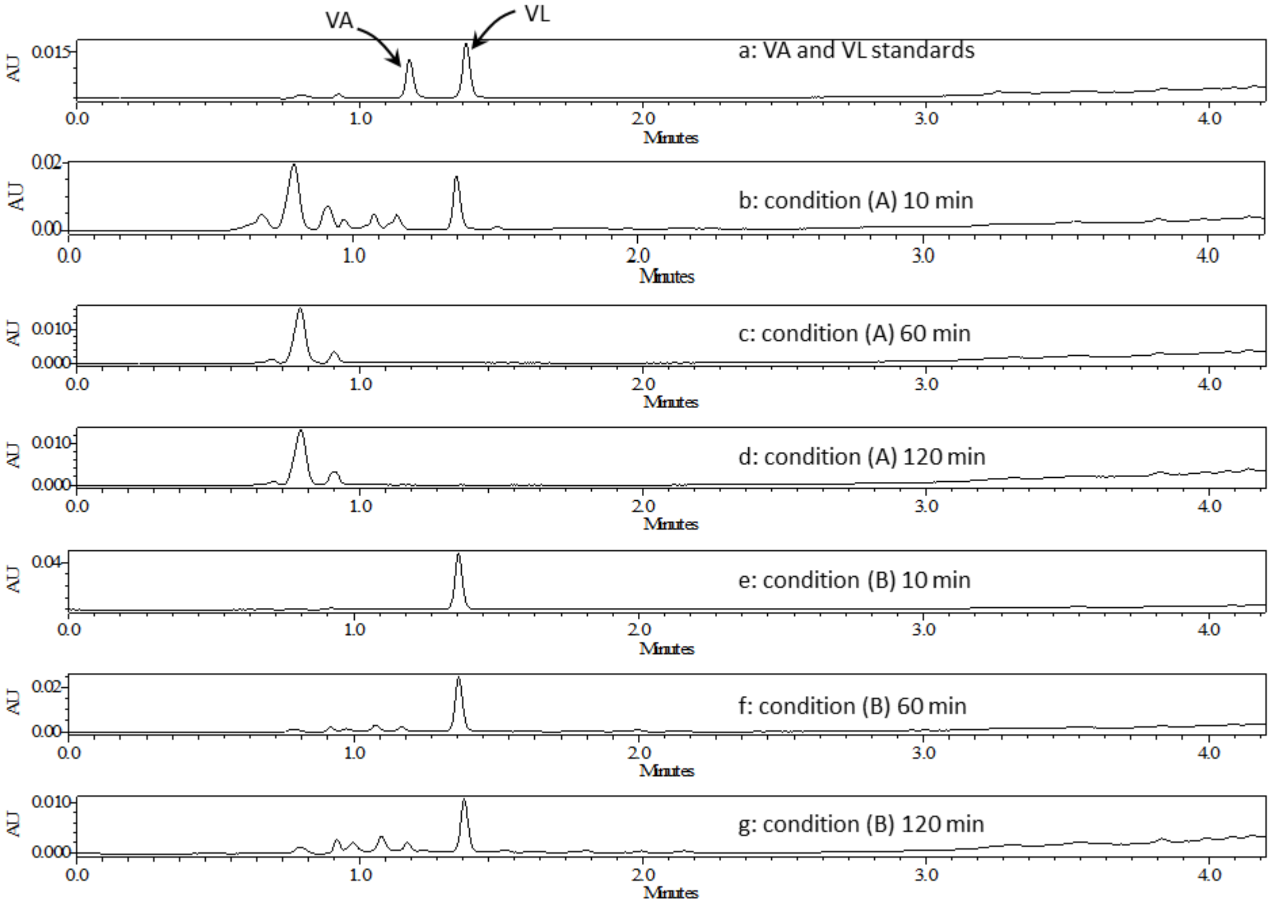

Figure S9. Typical chromatograms from the standards (a), samples in condition (A) at different time intervals (b-d), and samples in condition (B) at different time intervals (e-g).

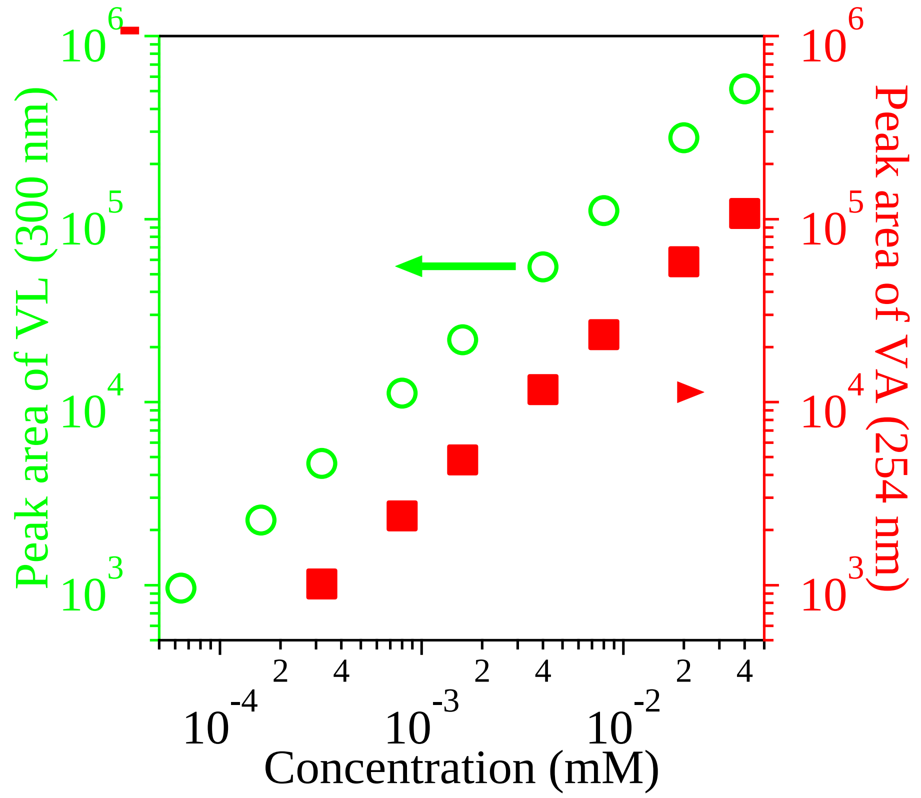

Figure S10. Typical calibration curves for VL (green) and VA (red) using UPLC-DAD.

5.2 Ultra-performance liquid chromatography electrospray ionization time-of-flight mass spectrometry (UPLC-ESI-ToF-MS)

Samples from A_9 and B_7 (Table 1) were collected at different time intervals. 10 µL of 1% hydrogen peroxide catalase were added to each sample from A_9 to destroy unreacted H_2O_2. A Waters ACQUITY UPLC system plus a Bruker Daltonics MirOTOF MS with an electrospray ionization (ESI) source was used for sample analysis. The UPLC column was a Waters ACQUITY UPLC HSS C18 column (2.1 × 100 mm, 1.8 µm). Mobile phases were 0.1% acetic acid in water (A) and 0.1% acetic acid in methanol (B). The gradient was 100% A in the first 2 minutes, decreased to 10% A in 28 minutes, stayed at 10% A until 42.2 minutes, and increased back to 100% A in 45 minutes. The flow rate was 0.2 mL/min. The ESI-MicrOTOF MS was operated under negative mode with a scanning *m*/*z* range of 50-1000. The capillary voltage was 4000 V, with an end plate offset of -500 V. The nebulizer pressure was 3.0 bar and the dry gas was at 4.0 L/min with dry heater operating at 220 °C. In-source collision induced dissociation, with a collision energy of -10.0 eV, was used to generate some fragments for structural elucidation.

Fragmentation information induced by in-source collision was used for structural elucidation. For example, we observed three peaks in the chromatogram (Figure S11) with m/z 167 ± 0.5 Da ($[M - H]^-$). The mass spectra of these three peaks are shown in Figure S12 (panel a-c). The spectrum in Figure S12-b has a loss of CO_2 (see also Table S3), a characteristic loss of carboxylic acids (Li et al., 2011a). This product is therefore believed to be a carboxylic acid, formed by oxidation in the carbonyl group of VL. The other two isobaric products do not have this CO_2 loss (Figures S11-a and -c, and Table S3), thus they are believed to be formed with one oxygen atom added to the aromatic ring as OH group. The positions of the OH group in these two products are not known at this point. Likewise, two isobaric products with a molecular weight of 184 ($[M-H]^- = 183$) are believed to be formed by adding one more oxygen atom to the above products. One of them (B184_a, Figure S12-d) is believed to be a carboxylic acid with one more OH group than B168_b, while the other has two OH groups added to the aromatic ring (Figure S11-e). The product B302_a is believed to be a dimer of VL by radical polymerization based on two reasons. First, the molecular formula ($C_{16}H_{14}O_6$) is double of that of VL ($C_8H_8O_3$) with two hydrogen atoms less, supporting a radical polymerization process (Sun et al., 2010). Second, the loss of two CH_3 groups (Table S3) suggests that there are two building blocks with VL structure that bears two OCH_3 groups contributing to the CH_3 losses. There is little information of other dimers for structural elucidation and their structures are not proposed.

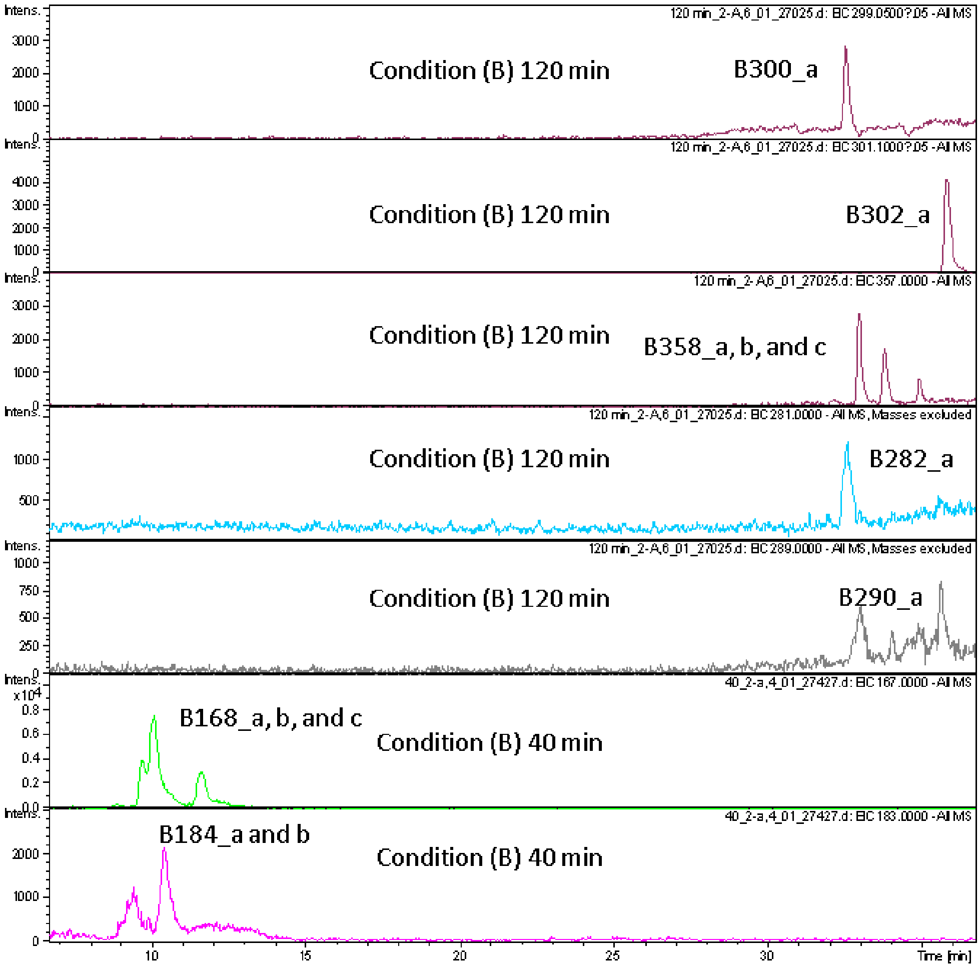

Figure S11. Extracted ion chromatograms (EIC) for samples from condition (B).

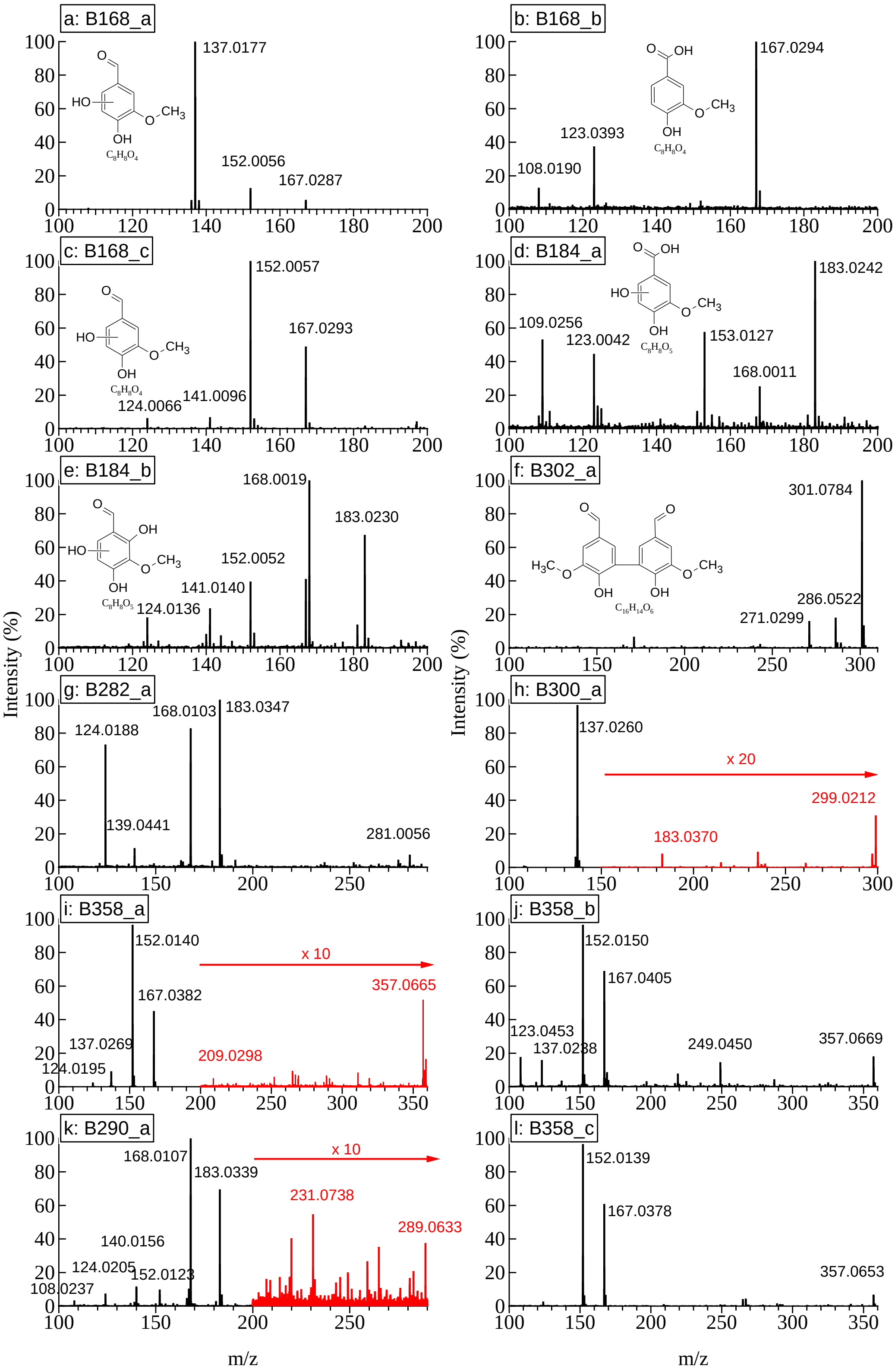

Figure S12. Mass spectra of products identified by UPLC-ESI-ToF-MS.

Table S3. Formulas, double bond equivalency, major ions, and fragmentation routes proposed for products identified by UPLC-ESI-ToF-MS. Note: ^{a} DBE = double bond equivalency; ^{b} Δ = measured – calculated; ^{c} possible fragmentation routes.

Name	**Formula**	**DBE^a**	**Ion peak**	**Measured**	**Calculated**	**Δ^b (mDa)**	**Loss^c**
B168_a	$C_8H_8O_4$	5	$C_8H_7O_4^-$	167.0287	167.0344	-5.7	$-H$
			$C_7H_4O_4^-$	152.0056	152.0110	-5.4	$-H-CH_3$
			$C_7H_5O_3^-$	137.0177	137.0239	-6.2	$-H-CH_2O$
B168_b	$C_8H_8O_4$	5	$C_8H_7O_4^-$	167.0294	167.0344	-5.0	$-H$
			$C_7H_7O_2^-$	123.0393	123.0446	-5.3	$-H-CO_2$
			$C_6H_4O_2^-$	108.0190	108.0211	-2.1	$-H-CH_3-CO_2$
B168_c	$C_8H_8O_4$	5	$C_8H_7O_4^-$	167.0293	167.0344	-5.1	$-H$
			$C_7H_4O_4^-$	152.0057	152.0110	-5.3	$-H-CH_3$
			$C_6H_5O_4^-$	141.0096	141.0188	-9.2	$-H-C_2H_2$
			$C_6H_4O_3^-$	124.0066	124.0160	-9.4	$-H-CH_3-CO$
B184_a	$C_8H_8O_5$	5	$C_8H_7O_5^-$	183.0242	183.0293	-5.1	$-H$
			$C_7H_4O_5^-$	168.0011	168.0058	-4.7	$-H-CH_3$
			$C_7H_5O_4^-$	153.0127	153.0188	-6.1	$-H-CH_2O$
			$C_6H_3O_3^-$	123.0042	123.0082	-4.0	$-H-C_2H_4O_2$
			$C_6H_5O_2^-$	109.0256	109.0290	-3.4	$-H-CH_2O-CO_2$
B184_b	$C_8H_8O_5$	5	$C_8H_7O_5^-$	183.0230	183.0293	-6.3	$-H$
			$C_7H_4O_5^-$	168.0019	168.0058	-3.9	$-H-CH_3$
			$C_7H_4O_4^-$	152.0052	152.0110	-5.8	$-H-CH_3O$
			$C_6H_5O_4^-$	141.0140	141.0188	-4.8	$-H-C_2H_2O$
			$C_6H_4O_3^-$	124.0136	124.0160	-2.4	$-H-CH_3O-CO$
B302_a	$C_{16}H_{14}O_6$	10	$C_{16}H_{13}O_6^-$	301.0784	301.0712	7.2	$-H$
			$C_{15}H_{10}O_6^-$	286.0522	286.0477	4.5	$-H-CH_3$
			$C_{14}H_7O_6^-$	271.0299	271.0243	5.6	$-H-CH_3-CH_3$
B282_a	$C_{15}H_6O_6$	13	$C_{15}H_5O_6^-$	281.0056	281.0086	-3.0	$-H$
B300_a	$C_{15}H_8O_7$	12	$C_{15}H_7O_7^-$	299.0212	299.0192	2.0	$-H$
B358_a	$C_{16}H_{16}O_8$	9	$C_{16}H_{14}NaO_8^-$	357.0665	357.0586	7.9	$-2H+Na^+$
B358_b	$C_{16}H_{16}O_8$	9	$C_{16}H_{14}NaO_8^-$	357.0669	357.0586	8.3	$-2H+Na^+$
B290_a	$C_{15}H_{14}O_6$	9	$C_{15}H_{13}O_6^-$	289.0633	289.0712	-7.9	$-H$
B358_c	$C_{16}H_{16}O_8$	9	$C_{16}H_{14}NaO_8^-$	357.0653	357.0586	6.7	$-2H+Na^+$

5.3 Gas chromatography mass spectrometry (GC-MS) with derivatization

Using the BF_3/butanol method, samples from A_9 and B_7 or standard compounds (glyoxylic acid, oxalic acid, malonic acid and pyruvic acid, from Sigma-Aldrich) in aqueous phase were adjusted to pH = 8.5~9.5 using a 0.1 M NaOH (AR grade, Sigma-Aldrich) solution. The 5-mL samples were first concentrated to approximately 0.5 mL using a rotary evaporator under vacuum, then transferred to a 4-mL graduated conical vial and further concentrated to dryness under a nitrogen stream. A total volume of 0.25 mL of 10% BF_3/1-butanol (Supelco, Bellefonte, PA, USA) was immediately added to the sample. The samples and reagents were mixed with ultrasonication for 1 minute and then heated at 100 °C for 30 minutes to form butyl ester for the carboxyl group and acetal for the aldehyde group. Once the sample cooled down, the derivatives were extracted with hexane (95%, Mallinckrodt) (5 × 1 mL) after adding 0.3 mL of acetonitrile (ACN, 99.8%, Duksan) and 3 mL of deionized water. The fractions were combined and further washed with deionized water (3 × 3 mL). Then, the resulting solutions were dried over anhydrous Na_2SO_4 (AR grade, Sigma-Aldrich) and concentrated to about 250 µL by a nitrogen stream.

The resulting derivatives were injected into a GC-MS system (Perkin-Elmer Clarus 500) for analysis. The temperature program was set to a constant 40 °C for 4 minutes, increased to 200 °C at the rate of 8 °C/min and held for 0 minutes, then further to 300 °C at 20 °C/min and finally maintained at 300 °C for 1 minute. The injection volume was 10 µL. The MS data (total ion chromatogram) were acquired in the full scan mode (m/z of 50–600) using electron ionization. The solvent delay was set to 5 minutes.

Using the pentafluorophenylhydrazine (PFPH) method, the aqueous-phase samples from A_9 and B_7 or standard compounds (formaldehyde and glyoxal) were adjusted to pH=8.5~9.5 with the help of a 0.1 M NaOH solution. The 5-mL samples were first concentrated to approximately 1 mL using a rotary evaporator under vacuum, then transferred to a vial upon which 1 mL of 0.5 mM PFPH (Sigma-Aldrich, 97%) aqueous solution was immediately added. The mixtures were left to react at room temperature in the dark overnight. Later, 5 × 2 mL hexane was used to extract the derivatives, followed by drying with anhydrous Na_2SO_4 and filtering. The extract was concentrated to about 200 µL before the GC-MS analysis. The GC-MS conditions were the same as those when the BF_3/butanol method was used.

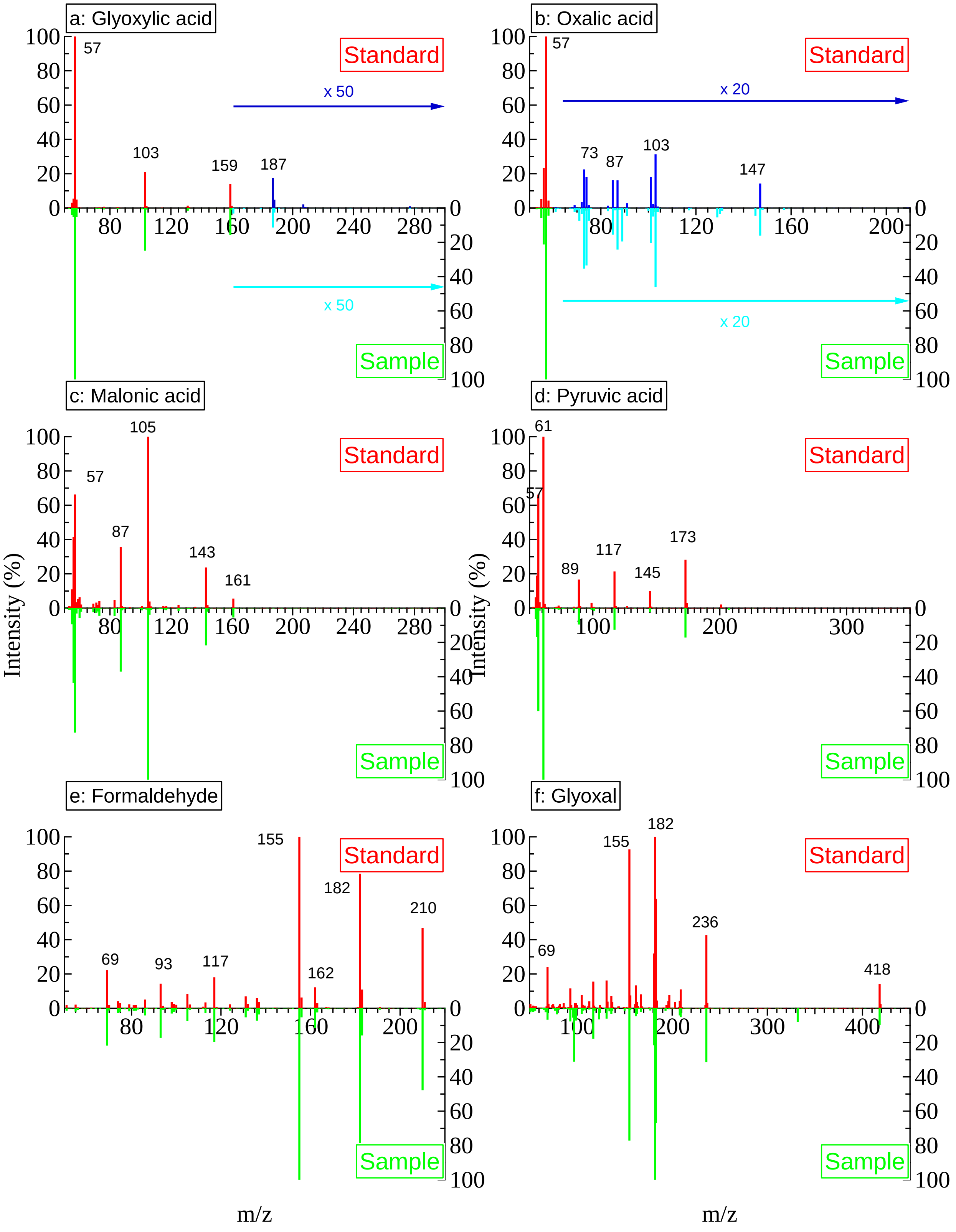

Figure S13. Mass spectra of standard compounds (red) and of products from the samples (green) identified by GC-MS. BF2/butanol method: a – d; PFPH method: e and f.

6. Estimated organic growth factor at 90% RH

The organic growth factors (GF_{org}) were calculated from the measured GF_{90} by assuming a constant GF of ammonium sulfate (AS) of 1.68. They were calculated based on the ZSR rule (Seinfeld and Pandis, 2006) as in Eq. 1 below, with GF_{org} being the GF of organics, GF_{AS} the GF of AS, ε_{org} the volume fraction of organics, and ε_{AS} the volume fraction of AS.

$$GF_{org} = \sqrt[3]{\frac{GF_{90}^3 - GF_{AS}^3 \times \varepsilon_{AS}}{\varepsilon_{org}}} \qquad \text{Eq. S1}$$

The volume fraction of organics (ε_{org}) was calculated based on the mass fraction of organics measured by the AMS, and the density estimated from H:C and O:C ratios (Kuwata et al., 2012) as shown below.

$$\rho_{org} = 1000 \times \frac{12 + H{:}C + 16 \times O{:}C}{7.0 + 5.0 \times H{:}C + 4.15 \times O{:}C} \qquad \text{Eq. S2}$$

$$\varepsilon_{org} = \frac{\frac{f_{org}}{\rho_{org}}}{\left(\frac{f_{org}}{\rho_{org}} + \frac{f_{AS}}{\rho_{AS}}\right)} \qquad \text{Eq. S3}$$

$$\varepsilon_{AS} = 1 - \varepsilon_{org} \qquad \text{Eq. S4}$$

where ρ_{org} (kg/m^3) is the density of organics, H:C and O:C are the hydrogen-to-carbon ratio and the oxygen-to-carbon ratio, respectively, of organics, f_{org} and f_{AS} are the mass fractions of AMS-measured organics and sulfate, respectively, and ρ_{AS} =1769 kg/m^3 is the density of ammonium sulfate.

7. Estimation of photolysis rate in 295-425 nm

Wavelength-dependent photolysis rate (J) can be estimated from the absorption cross section ($\sigma(\lambda)$), the quantum yield ($\phi(\lambda)$), and the solar actinic flux ($I(\lambda)$), all of which are wavelength dependent (Seinfeld and Pandis, 2006). The first two parameters, $\sigma(\lambda)$ and $\phi(\lambda)$, are also compound specific and are not readily available in the literature for VL. The last parameter, $I(\lambda)$, can be estimated from the energy output of the UV lamp (UVP, Pen-ray 254 nm 9", model 97606-08) used in the experiments and from literature for typical tropospheric environments (Finlayson-Pitts and Pitts, 1986).

We first estimate J_{VL} in our experiments under condition (B), assuming that the decay of VL under condition (B) was solely due to direct photolysis. Then we have (Seinfeld and Pandis, 2006):

$$\frac{d[VL]}{dt} = -k_{decay} \times [VL] = -J_{VL} \times [VL]$$

$$J_{VL} = \int \sigma_{VL}(\lambda)\phi_{VL}(\lambda)I(\lambda)d\lambda = \sum \bar{\sigma}_{VL}(\lambda)\bar{\phi}_{VL}(\lambda)\bar{I}(\lambda)\Delta\lambda$$

where k_{decay} is our measured decay rate (s^{-1}) under condition (B), J_{VL} is the first-order photolysis rate (s^{-1}) of VL, $\sigma_{VL}(\lambda)$ is the wavelength-dependent absorption cross section (cm^2) of VL, $\phi_{VL}(\lambda)$ is the wavelength-dependent quantum yield of VL, and $I(\lambda)$ is the solar actinic flux, or the photo flux from the UV lamp in our experiments. The integration is simplified by summing the photolysis rates in finite "bins" (with $\Delta\lambda = 5\ nm$), calculated from the average values of the required parameters (denoted by a bar over the symbols).

Absorption cross section can be estimated from molar absorption coefficient:

$$\sigma_{VL}(\lambda) = \frac{10^3 \times \varepsilon_{VL}(\lambda)}{N_A}$$

where $\varepsilon_{VL}(\lambda)$ is the molar absorption coefficient ($dm^3/mol/cm$) and N_A is the Avogadro constant ($6.02 \times 10^{23}\ mol^{-1}$). Figure S14-a shows the molar absorption coefficient (from NIST) of VL from 220-350 nm in a red line (Talrose et al., 2007), and the calculated absorption cross section ($\sigma_{VL}(\lambda)$, 290-425 nm, $\Delta\lambda$=5 nm) is shown as blue open symbols in Figure S14-a. The molar absorption coefficient beyond 350 nm, which is not included in NIST database, was assumed to decrease exponentially from 330 nm without major absorption band in this region for VL.

Absorption cross section for experiments under condition (B) is thus calculated.

$$\bar{\sigma}_{VL}(254) = 2.35 \times 10^{-20} cm^2$$

The quantum yield during experiments under condition (B), $\bar{\phi}_{VL}(254)$, is first assumed to be unity. Photon flux is calculated from the energy output (F_{UV}, specified by the manufacturer) of the UV lamp, $F_{UV} = 5.4\ mW/cm^2 = 5.4 \times 10^{-3}\ J\ cm^{-2}\ s^{-1}$, at 0.75 inch (approximately half of the bottle radius), by:

$$\bar{I} = \frac{F_{UV}}{E_{hv}} = \frac{F_{UV}}{\frac{h \times c}{\lambda}} = \frac{5.4 \times 10^{-3} Jcm^{-2}s^{-1}}{\frac{6.626 \times 10^{-34} J \cdot s \times 2.998 \times 10^{8}\ m\ s^{-1}}{254 \times 10^{-9}\ m}} = 6.92 \times 10^{15} photons\ cm^{-2}s^{-1}$$

Here E_{hv} is the energy of one photon, h is the Planck constant and c is the speed of light. The estimated J_{VL} at 254 nm in our experiments is (assuming quantum yield of 1 $photon^{-1}$ and wavelength width of

5 nm):

$$J_{VL}(254) = \bar{\sigma}_{VL}(\lambda)\bar{\phi}_{VL}(\lambda)\bar{I}(\lambda)\Delta\lambda = 6.92\ \times\ 10^{15}\ photons\ cm^{-2}s^{-1} \times 2.35 \times 10^{-20}cm^{2} \times 1 \times 5$$
$$= 8.13 \times 10^{-4}s^{-1}$$

This estimated $J_{VL}(254)$ is 3.5 times of the measured k_{decay} (2.3 × 10^{-4} s^{-1}) in our experiments under condition (B). We attribute this difference to the quantum yield of VL photolysis and hence assume a non-unity quantum yield for the whole wavelength:

$$\bar{\phi}_{VL}(\lambda) = \frac{2.3 \times 10^{-4}}{8.13 \times 10^{-4}} = 0.28.$$

Using this quantum yield, we then estimate the photolysis rates of VL in the UV region of tropospheric importance (290-425 nm). The wavelength-dependent solar actinic flux in typical tropospheric environments (ground level, July 1, noon, 40°N, 298 K) is taken from (Finlayson-Pitts and Pitts, 1986) and is shown in red open symbols in Figure S14-b.The estimated photolysis rates are believed to be upper limits since wavelength-dependent quantum yields normally decrease, most likely exponentially, as wavelength increases.

Table S4 showed the estimated photolysis rates of VL in different wavelength “bins”. The photolysis rates of VL range from 10^{-5} to 10^{-4} s^{-1} for wavelength where VL has a strong absorption band, i.e., 300-350 nm. Beyond 350 nm, the photolysis rates become too small to be important due to low absorption cross section for VL. The overall J_{VL} is 7.06 × 10^{-4} s^{-1}, a few times higher than the k_{decay} measured (2.3 × 10^{-4} s^{-1}) and the gas-phase loss rate due to OH reactions (1 × 10^{-4} s^{-1}). Therefore, we believe that the decay rate due to UV photolysis of VL in the troposphere is at least comparable to that of OH reactions in gas phase. Note that the same UV photolysis can occur in gas phase too.

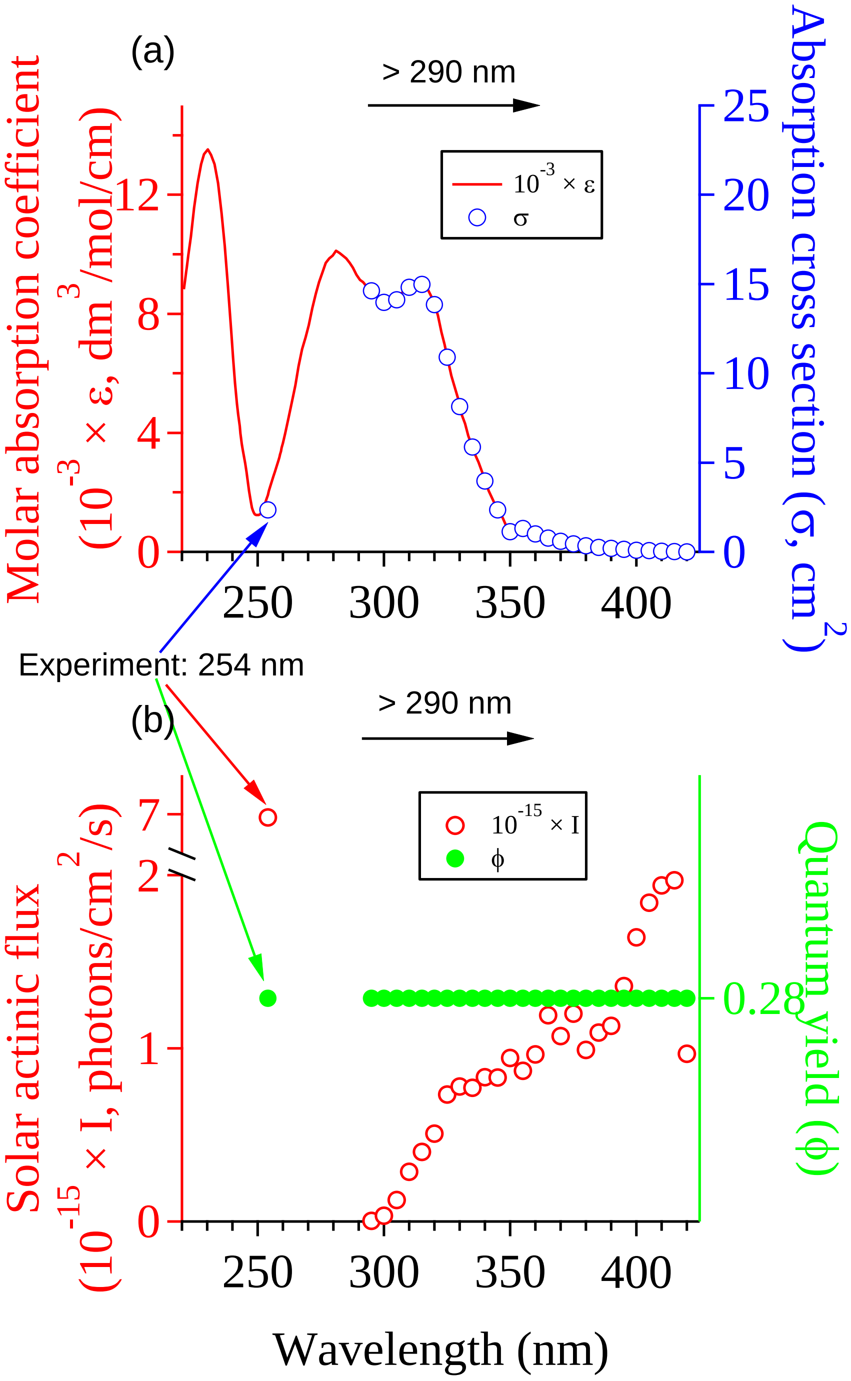

Figure S14. (a) molar absorption coefficient (from NIST database) and estimated absorption cross section of VL; (b) solar actinic flux in typical tropospheric environments: ground level, July 1, noon, 40°N, 298 K (Finlayson-Pitts and Pitts, 1986) and assumed quantum yield (0.28) for VL.

Table S4. Estimation of wavelength-dependent photolysis rates of VL.

Wavelength λ (nm)	$\bar{I}$ **(photons cm^{-2} s^{-1})**	$10^{20} \times \bar{\sigma}_{VL}$ **(cm^{2})**	$\bar{\phi}_{VL}$	J_{VL} **(s^{-1})**
254 (condition B)	**6.92×10^{15}**	**2.35**	**0.28**	**2.3×10^{-4}**
295-300	3.14×10^{12}	15	0.28	6.42×10^{-7}
300-305	3.35×10^{13}	14	0.28	6.56×10^{-6}
305-310	1.24×10^{14}	14	0.28	2.45×10^{-5}
310-315	2.87×10^{14}	15	0.28	5.96×10^{-5}
315-320	4.02×10^{14}	15	0.28	8.43×10^{-5}
320-325	5.08×10^{14}	14	0.28	9.85×10^{-5}
325-330	7.34×10^{14}	11	0.28	1.12×10^{-4}
330-335	7.79×10^{14}	8.1	0.28	8.88×10^{-5}
335-340	7.72×10^{14}	5.9	0.28	6.34×10^{-5}
340-345	8.33×10^{14}	4	0.28	4.63×10^{-5}
345-350	8.32×10^{14}	2.4	0.28	2.74×10^{-5}
350-355	9.45×10^{14}	1.1	0.28	1.49×10^{-5}
355-360	8.71×10^{14}	1.3	0.28	1.59×10^{-5}
360-365	9.65×10^{14}	1	0.28	1.36×10^{-5}
365-370	1.19×10^{15}	0.78	0.28	1.30×10^{-5}
370-375	1.07×10^{15}	0.6	0.28	8.95×10^{-6}
375-380	1.20×10^{15}	0.46	0.28	7.67×10^{-6}
380-385	9.91×10^{14}	0.35	0.28	4.81×10^{-6}
385-390	1.09×10^{15}	0.26	0.28	3.97×10^{-6}
390-395	1.13×10^{15}	0.19	0.28	3.05×10^{-6}
395-400	1.36×10^{15}	0.14	0.28	2.66×10^{-6}
400-405	1.64×10^{15}	0.099	0.28	2.26×10^{-6}
405-410	1.84×10^{15}	0.066	0.28	1.71×10^{-6}
410-415	1.94×10^{15}	0.041	0.28	1.11×10^{-6}
415-420	1.97×10^{15}	0.021	0.28	5.85×10^{-7}
420-425	9.69×10^{14}	0.0057	0.28	7.78×10^{-8}
Total (295-425 nm)				**7.06×10^{-4}**

8. References

Aiken, A. C., DeCarlo, P. F., and Jimenez, J. L.: Elemental analysis of organic species with electron ionization high-resolution mass spectrometry, Anal. Chem., 79, 8350-8358, 2007.

Allan, J. D., Delia, A. E., Coe, H., Bower, K. N., Alfarra, M. R., Jimenez, J. L., Middlebrook, A. M., Drewnick, F., Onasch, T. B., Canagaratna, M. R., Jayne, J. T., and Worsnop, D. R.: A generalised method for the extraction of chemically resolved mass spectra from aerodyne aerosol mass spectrometer data, J. Aerosol Sci., 35, 909-922, 2004.

Allen, A. O., Hochanadel, C. J., Ghormley, J. A., and Davis, T. W.: Decomposition of water and aqueous solutions under mixed fast neutron and gamma-radiation, J. Phys. Chem., 56, 575-586, 1952.

An, Y. J., Jeong, S. W., and Carraway, E. R.: Micellar effect on the photolysis of hydrogen peroxide, Water Res., 35, 3276-3279, 2001.

Chen, Q., Liu, Y. J., Donahue, N. M., Shilling, J. E., and Martin, S. T.: Particle-Phase Chemistry of Secondary Organic Material: Modeled Compared to Measured O:C and H:C Elemental Ratios Provide Constraints, Environ. Sci. Technol., 45, 4763-4770, 2011.

Ervens, B., Turpin, B. J., and Weber, R. J.: Secondary organic aerosol formation in cloud droplets and aqueous particles (aqSOA): a review of laboratory, field and model studies, Atmos. Chem. Phys., 11, 11069-11102, 2011.

Ervens, B., Wang, Y., Eagar, J., Leaitch, W. R., Macdonald, A. M., Valsaraj, K. T., and Herckes, P.: Dissolved organic carbon (DOC) and select aldehydes in cloud and fog water: the role of the aqueous phase in impacting trace gas budgets, Atmos. Chem. Phys., 13, 5117-5135, 2013.

Finlayson-Pitts, B. J., and Pitts, J. N. J.: Atmospheric Chemistry: Fundamentals and Experimental Techniques, Wiley, New York, 1986.

Kuwata, M., Zorn, S. R., and Martin, S. T.: Using Elemental Ratios to Predict the Density of Organic Material Composed of Carbon, Hydrogen, and Oxygen, Environ. Sci. Technol., 46, 787-794, 2012.

Lee, A. K. Y., Hayden, K. L., Herckes, P., Leaitch, W. R., Liggio, J., Macdonald, A. M., and Abbatt, J. P. D.: Characterization of aerosol and cloud water at a mountain site during WACS 2010: secondary organic aerosol formation through oxidative cloud processing, Atmos. Chem. Phys., 12, 7103-7116, 2012.

Li, Y. J., Chen, Q., Guzman, M. I., Chan, C. K., and Martin, S. T.: Second-generation products contribute substantially to the particle-phase organic material produced by beta-caryophyllene ozonolysis, Atmos. Chem. Phys., 11, 121-132, 2011a.

Li, Y. J., Yeung, J. W. T., Leung, T. P. I., Lau, A. P. S., and Chan, C. K.: Characterization of Organic Particles from Incense Burning Using an Aerodyne High-Resolution Time-of-Flight Aerosol Mass Spectrometer, Aerosol Sci. Technol., 46, 654-665, 2011b.

Seinfeld, J. H., and Pandis, S. N.: Atmospheric chemistry and physics: From air pollution to climate change, 2nd ed., Wiley, New Jersey, 2006.

Sun, Y. L., Zhang, Q., Anastasio, C., and Sun, J.: Insights into secondary organic aerosol formed via aqueous-phase reactions of phenolic compounds based on high resolution mass spectrometry, Atmos. Chem. Phys., 10, 4809-4822, 2010.

Tan, Y., Perri, M. J., Seitzinger, S. P., and Turpin, B. J.: Effects of Precursor Concentration and Acidic Sulfate in Aqueous Glyoxal-OH Radical Oxidation and Implications for Secondary Organic Aerosol, Environ. Sci. Technol., 43, 8105-8112, 2009.

Warneck, P.: In-cloud chemistry opens pathway to the formation of oxalic acid in the marine atmosphere, Atmos. Environ., 37, 2423-2427, 2003.

Zhang, Q., Canagaratna, M. R., Jayne, J. T., Worsnop, D. R., and Jimenez, J. L.: Time- and size-resolved chemical composition of submicron particles in Pittsburgh: Implications for aerosol sources and processes, J. Geophys. Res.-Atmos., 110, D07S09, doi:10.1029/2004JD004649, 2005.